The International Journal of Advanced Manufacturing Technology (2020) 107:3499–3510
https://doi.org/10.1007/s00170-020-05255-4

ORIGINAL ARTICLE

In situ fatigue monitoring investigation of additively manufactured maraging steel

T. C. Henry[1] · F. R. Phillips[1] · D. P. Cole[1] · E. Garboczi[2] · R. A. Haynes[1] · T. Johnson[1]

Received: 11 December 2019 / Accepted: 30 March 2020 / Published online: 17 April 2020

Abstract
This work describes an experimental validation set for assessing the real-time fatigue behavior of metallic additive manufacturing (AM) maraging steel structures. Maraging steel AM beams were fabricated with laser powder bed fusion (LPBF) and characterized with ex situ studies of porosity through X-ray computed tomography (CT), nano-indentation, and atomic force microscopy, as well as quasi-static testing to evaluate the as-printed state. Microscale evaluation showed void content of 0.34–0.36% with hardness and stiffness variation through the build direction on the order of 5.1–5.6 GPa and 139–154 GPa, respectively. The microscale inhomogeneities created an as-printed state where the compression and tension plasticity behavior at the macroscale was unequal in quasi-static loading, leading to greater yielding in tension. Specimens were subjected to cyclic loads, while the structural behavior was characterized through in situ magnetic permeability, digital image correlation (DIC) strain, and structural compliance measurements. In the range of 3×10^3 to 3×10^4 cycles to failure, magnetic permeability measurements were able to capture the mechanical state as early as 60% of life depending on failure location. Results are discussed with an emphasis on material-property-structure relationships in terms of the multi-scale material state and fatigue validation data for improving the durability of AM parts.

Keywords Additive manufacturing · AM · Digital image correlation · DIC · Nano-indentation · X-ray computed tomography · Fatigue

1 Introduction

Additive manufacturing (AM) processes are attractive to designers because they require little tooling, taking a virtual design and replicating it in an automated layered process. Parts can be complex with some considerations for artifacts like overhangs or trapped unprocessed material. AM processes have matured to the point where they are structurally relevant even if there is some uncertainty in the mechanical and fatigue behavior, especially for newly developed polymers and alloys [1]. Use of AM technologies for primary load-bearing structures requires certainty in the fatigue response by ensuring understanding via validation of simulations based on representative experiments. Uncertainty in fatigue response in terms of deviation print-to-print or print compared with design will typically result in structures with larger factors of safety. A more optimal and lighter-weight AM design could be realizable even with uncertainty by monitoring a signal against fatigue response ensuring safety via intervention when it can be reported that few cycles are remaining.

Research focused on fatigue response in AM technologies has shown that bulk properties are sensitive to defects [2, 3] and microstructure [4, 5]. Although not too different than other manufacturing methods in bulk tension or compression testing, ultimate failure by crack growth [6–9] or fatigue [10–12] loading in AM structures has shown degraded performance compared with identical structures made by other manufacturing techniques [13]. This reduction in performance is due to the way damage nucleates around microstructural defects and material differences caused by the printing process (e.g., manufacturing variability) [14–20]. Laser manufacturing processes can appear to be visually homogeneous, although micrographs can reveal uneven growth of fine grains

✉ T. C. Henry
todd.c.henry2.civ@mail.mil

[1] Vehicle Technology Directorate, U.S. Army Research Laboratory, 6340 Rodman Road B4603, APG, MD 21005, USA

[2] Material Measurement Laboratory, National Institute of Standards and Technology, 325 Broadway MS 647, Boulder, CO 80305, USA

and the remnant boundaries of different melt pools [21, 22], which can influence fatigue. When building up a larger structure with designed intricate features [23–28], understanding the defect characteristics of the material is necessary to avoid unexpected failures.

The uncertain nature of fatigue performance for AM technologies can be mitigated with monitoring of the structural state, particularly with methods that are sensitive to the actual defects that instigate early failure. Experimental methods such as nano-indentation [29, 30], atomic force microscopy, and X-ray computed tomography are capable of evaluating very small quantities of material even between AM layers. Measurements of local porosity, modulus, and hardness have been shown to be indicators of failure nucleation as well as fatigue damage and failure in methods other than AM [31–33]. The influence of small-scale damage on larger-scale measurements such as dynamic vibration [34–36], ultrasound [37, 38], stiffness degradation [39, 40], and eddy current [41–43] can be sensitive to that damage when the scattering of the measurement energy is great enough. The signal response from the sensor can then be used to track the state of the material and estimate impending failure, creating an opportunity for a user to intercede and limit catastrophic fatigue failures.

A fundamental understanding of the printed state and in situ damage evolution is required to predict the fatigue behavior of seemingly identical specimens. Information from experimental investigation is required to validate accurate multi-scale models and successfully design more complex architectures. The goal of this work is to provide digital image correlation (DIC), structural compliance, and eddy current magnetic permeability in situ measurements for characterizing the fatigue behavior of AM maraging steel. First, measurements of porosity via X-ray computed tomography, nano-indentation modulus and hardness, and atomic force microscopy topography are reported to give an understanding of the microscale state. Second, quasi-static experiments are conducted to capture the stress-strain-magnetic permeability behavior of the AM maraging steel beams. Third, beams were subjected to fatigue loading and monitoring results are presented with an emphasis on measurement signal vs. the number of fatigue cycles.

2 Materials and methods

Fifteen test specimens were made using an EOS M270 Dual Machine for laser powder bed fusion (LPBF) with individual specimens grouped near the center of the build plate. Specimens were oriented left to right with respect to the machine front with a nitrogen gas flow left to right pulling condensate from the part during manufacture. A laser power of 200 W was used with a manufacturer recommended volume rate of 4.2 mm^3/s and target layer height of 50 μm. The manufacturer reports a typical achievable part accuracy of ± 50 μm with a maximum particle size of 63 μm measured by sieve analysis according to ASTM B214. The recommended scan speed and hatch spacing from the literature were 750 mm/s and 100 μm, respectively, with a scan strategy of striped hatching [44]. The maraging steel powder was a formulation of EOS in its virginal state corresponding to 18% Ni maraging 300 steel. Specimens were cut to the approximate dimensions of (L_p, w, t) 203 mm by 20.1 mm by 20.1 mm by wire electron discharge machine (EDM) on every face except the top, which did not need EDM since the thickness dimension was well-controlled by the LPBF process. The build direction (z axis) was aligned vertically to the 3D printer as shown in Fig. 1. Average specimen mass was 650 g, resulting in an average density of 7.93 g/cm^3. The standard deviation in geometric tolerance, mass, and density between specimens was about 1%.

3 Ex situ and in situ characterization approaches

Sections of material were extracted and prepared in the xy, yz, and xz planes for nano-indentation and atomic force microscopy such that measurements were made on interior surfaces. Each section was polished using a series of sand papers from 300 grit to 1200 grit followed by 9 μm and 3 μm silica suspension for 5 min at each step. Nano-indentation (NI) experiments were performed on each section with a Hysitron TI-950 TriboIndenter. The Berkovich diamond tip used had a radius of curvature of approximately 150 nm. The tip area function was calibrated on a fused quartz standard. A loading rate of 1 mN/s was used, followed by a 5-s hold time. At two positions on each section, five-by-five arrays of indents

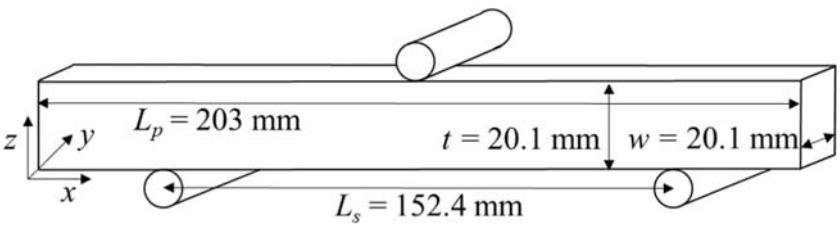

Fig. 1 Specimen test diagram with AM layered in the z direction. Every face was cut with wire EDM except for the top

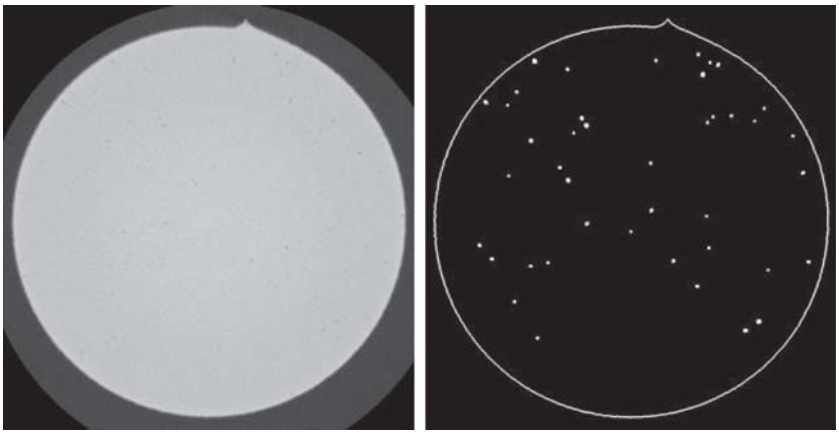

(a) (b)

Fig. 2 Sample X-ray CT output cross section of a cylindrical core. The sharp corner represents the start and end position of the wire EDM. **a** Original image. **b** Segmented image

spaced 7 μm apart were made in force control to a peak value of 10 mN. The indentation modulus was calculated assuming a sample Poisson's ratio of 0.3, tip elastic modulus of 1140 GPa, and tip Poisson's ratio of 0.07. Measurements of modulus and hardness usually have an uncertainty around 3%. Scanning probe measurements were performed using an Asylum MFP-3D atomic force microscope. The probes used in this study were AC160TS-R3 with a nominal natural frequency, stiffness, and tip radius of approximately 300 kHz, 26 N/m, and 10 nm, respectively. Imaging was performed in alternating contact mode at scan rates of approximately 1 Hz.

Ex situ X-ray CT scans were prepared on 5 mm diameter by 20 mm length cylinders taken with the length aligned with the z direction, using a wire EDM. Each scan used a voxel size of 6.432 μm/voxel, with a 160-kV tube voltage and a high-range filter, in order to get better transmission, on a Zeiss Versa XRM500 instrument. Four scans were used for each cylinder (A, B, C, D), to capture the entire 20 mm height of the cylinder, for a total of 12 scans and 12 fields of view (FOV). After reconstruction, each FOV resulted in about 1000 slices normal to the height of each cylinder, and each slice image was about 1000 pixels × 1000 pixels. For each cylinder, these FOVs overlapped by approximately 1 mm along the cylinder's length. Since there were also cone-beam artifacts at the bottom and top of each field of view, certain slices were discarded so that the remaining slices approximately covered the entire cylinder. Each of the image stacks for cylinders 1 and 2 was 19.5 and 19.9 mm in height taking into account the number of slices used. Since there are three interfaces between scans (A-B, B-C, and C-D) where slices may be missing, the possible errors in unaccounted overlap volume (assuming the cylinder height is 20 mm) would be at a maximum around 1.12 mm or 174 slices, which is only about 4% of the 4000 total images.

Upon collection of the slice images from X-ray CT, each image was processed through a custom segmentation algorithm built in MATLAB in order to determine the location and volume fraction of open space within the cylinders. The segmentation algorithm combined a total of 31 images around the current image being analyzed in order to determine a relevant average image without local inhomogeneities. The edge of the specimen in the current image was found through use of the pixel gradient. Subsequently, the internal area of the current image was compared with the matching internal area for the average image in order to determine localized differences in pixel intensity. All pixels within the internal area of the specimen found to have a pixel intensity difference greater than a threshold value were identified as local damage areas. Furthermore, a void had to be identified in the same general area over two consecutive slices in order to be counted. It is acknowledged that this threshold and multi-layer segmentation algorithm may omit some defects that could otherwise be identified. However, this method was found to give good repeatability, high fidelity to manual segmentation results, and a high signal-to-noise ratio.

Quasi-static and fatigue mechanical loading was conducted on an MTS hydraulic test machine[1] in three-point bending. The rectangular specimen had a supported length (L_s) of 152.4 mm resting on 12.7 mm diameter supports. Static loading was done at a rate of 1 mm/min displacement control for three specimens. Time, displacement, and force data were recorded at 5 Hz by the MTS controller. Fatigue loading was controlled by applying a sinusoidal cyclic force command at 2 Hz with an R ratio of 0.1. Peak values of cyclic force were chosen from above to below the yield strength of the material to capture a wide range of material behaviors for 12 specimens. The MTS controller captured the peak and valley displacement value changes as the force signal was controlled.

[1] Certain commercial equipment and/or materials are identified in this report in order to adequately specify the experimental procedure. In no case does such identification imply recommendation or endorsement by the National Institute of Standards and Technology or the Army Research Laboratory, nor does it imply that the equipment and/or materials used are necessarily the best available for the purpose

Specimens were named with the convention S# where 1–3 were loaded statically and 4–15 were loaded in fatigue.

In situ eddy current measurements of relative magnetic permeability (μ_r) were collected using a Jentek Jet7 handheld eddy current array with an uncertainty of around 3%. Eddy current data was collected during the static loading at 5 Hz as well as during fatigue loading periodically at 320 Hz to capture the fatigue response with accumulated cycles. Ex situ measurements were taken on the *xy* plane with three channels of the array oriented in both *x* and *y* directions separately while the specimen was pristine and at rest. In situ fatigue measurements were oriented in the *y* direction, mounted at the center of the beam. The array was calibrated in air and on the hardened stainless steel bending fixture with a μ_r measurement on average of 62.1 (coefficient of variation C_v 0.9%).

In situ three-dimensional digital image correlation (DIC) was collected at 5 Hz by Correlated Solutions software via a pair of five megapixel Point Grey Research digital cameras during static loading. Data points were correlated across the surface with subset, step, and filter sizes of 61, 7, and 15, respectively. During fatigue loading, images were captured at peaks and valleys by controlling on the force signal from the MTS frame with the Correlated Solutions Fulcrum module every 50 cycles. DIC resolution is limited to 50–100 με.

4 Ex situ characterization results

The as-built material state was investigated with the scanning and image processing of X-ray CT images as mentioned previously. A sample cross-sectional image from cylinder 1 is shown in Fig. 2, along with the output after segmentation showing the boundary of the specimen as well as the internal defects identified by the segmentation algorithm.

Segmented images were stacked to show the entire scanned volume as shown in Fig. 3 for cylinder 1, where the blue indicates the specimen boundary and the red indicates the local voids throughout the cylinder. Generally, voids were observed to be spread evenly throughout the volume.

In order to obtain a quantitative perspective on the distribution of voids through each cylinder, the void volume fraction was analyzed per slice and is presented in Fig. 4. The data suggests that the internal void volume fraction for cylinders 1 and 2 remains approximately constant throughout the height of the build with a mean value of 0.36% (C_v 14.7%) for cylinder 1 and a mean value of 0.34% (C_v 13.7%) for cylinder 2.

Typical nano-indentation force-displacement behavior is shown in Fig. 5a. Hardness measurements were on average 5.4 GPa (C_v 3.15%) across all faces with the highest measurement 5.6 GPa (C_v 3.04%) at $z = 20$ mm (*yz* plane) and the lowest measurement 5.1 GPa (C_v 2.49%) at $z = 0$ mm (*yz* plane) (Fig. 6). The indentation elastic modulus was calculated following the techniques outlined by Oliver and Pharr,

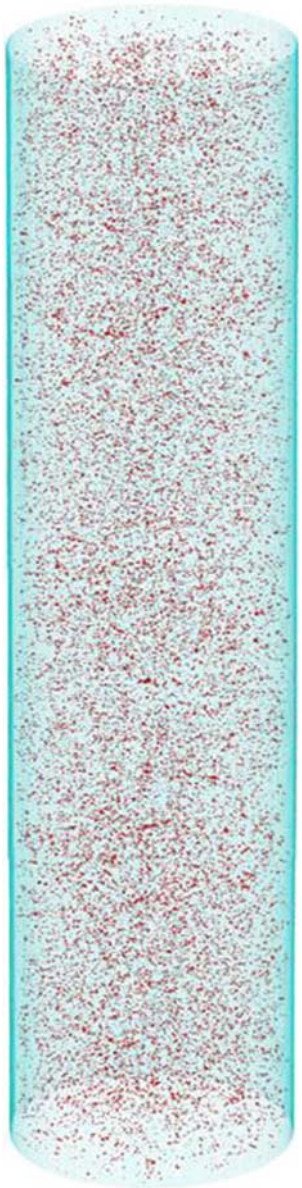

Fig. 3 Total volume image of cylinder sample 1. Blue shows specimen boundary and red shows local voids throughout specimen

which assume the samples are homogeneous, isotropic, and semi-infinite half spaces [45]. Interpretation of the modulus results is therefore somewhat qualitative due to the anisotropic nature of the material. Similar to the hardness measurement, the indentation modulus measurement was higher at $z = 20$ mm (154 GPa, C_v 2.92%) compared with $z = 0$ mm (139 GPa, C_v 3.60%). The lowest indentation modulus measurement was in the *xy* plane (121 GPa, C_v 4.16%). Sections of material were taken interior to the wire EDM cut; however, when taking indentation data at $z = 0$ mm or $z = 20$ mm on the *yz* plane, the material is likely influenced by the wire EDM which removes the specimen from the build plate.

Variations in the local nano-indentation measurements could be due to differences in residual stress [46] as evidenced

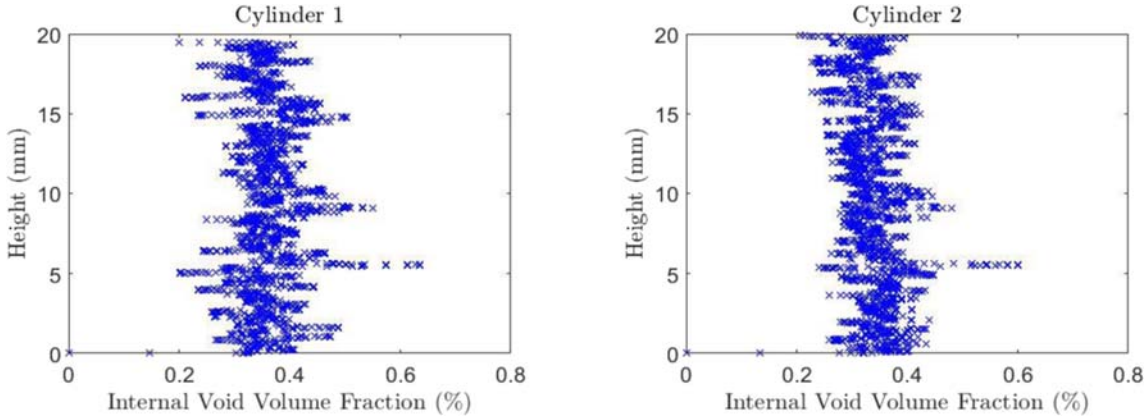

Fig. 4 Percentage of internal voids in each slice of material as identified based on segmentation of X-ray CT images. Each point represents the value of a slice

by AFM scans of pileup; however measurements can also influenced by grain sizes and the cutting and polishing process. Residual stress can cause dislocations to pile up (compressive stress) or sink in (tensile stress) around the indentation probe and affect the contact area measurement and thus the microscale mechanical behavior. Scanning probe microscopy was used to confirm the presence of pileup around the residual indentations. Figure 6 shows typical indentation arrays on the *yz* face near the top ($z = 20$ mm) and bottom ($z = 0$ mm) of the build direction. The residual indents near $z = 20$ mm displayed a higher degree of pileup with respect to the indentations on the other faces, and thus corresponds to the relatively high measured mechanical response. Variations in residual stress are common as a function of distance from the build plate and can contribute to structural heterogeneity as well as the fact that only the surface at $z = 0$ mm was cut by wire EDM, so that re-melt may effect measurements of modulus and hardness.

The two primary characteristics captured in ex situ testing were a porosity distribution of 0.34–0.36% and variation of mechanical properties in the build direction. Accurate representation of both aspects in simulation will have impact on predicted macroscale behavior and fatigue damage development.

5 In situ characterization results

5.1 Static loading

The *xy* plane relative magnetic permeability (μ_r), as measured under the top support, was on average 175.1 (C_v 3.6%) aligned in the *y* direction and 128.4 (C_v 3.0%) aligned in the *x* direction when specimens were unloaded. When under load, μ_r falls by around 130–140 to a minimum value near yielding and then slowly rises with displacement (Fig. 7). It should be noted that under static loading, the largest change in μ_r occurs

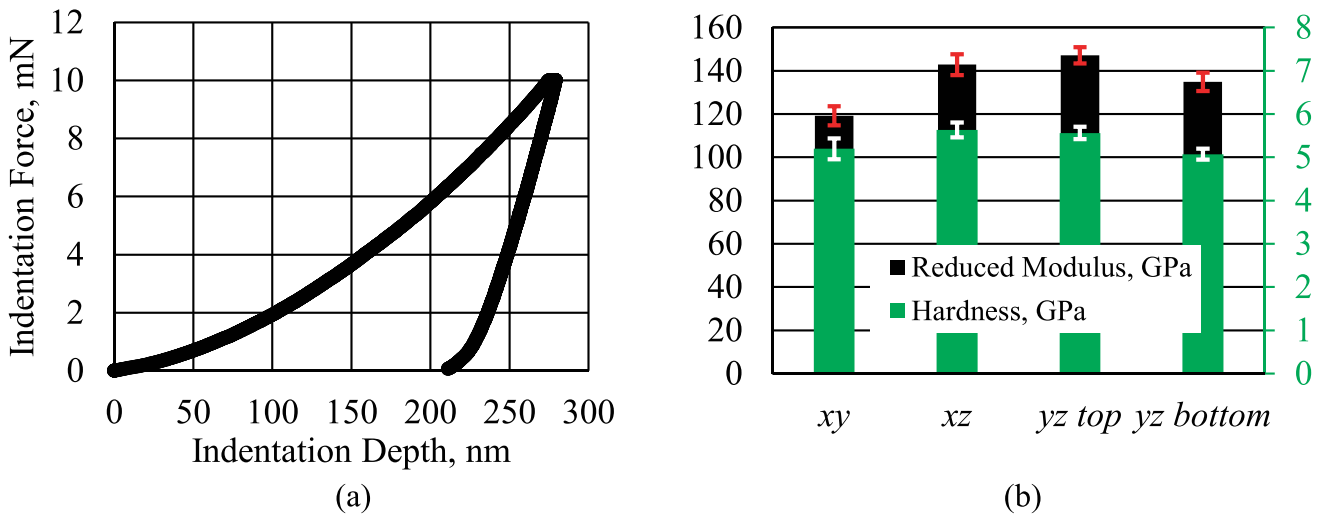

Fig. 5 Nano-indentation response as a function of sectioned plane **a** Typical force-displacement data for an indent in the x-y plane. **b** Indentation modulus (GPa) and hardness (GPa) for each polished face as measured from

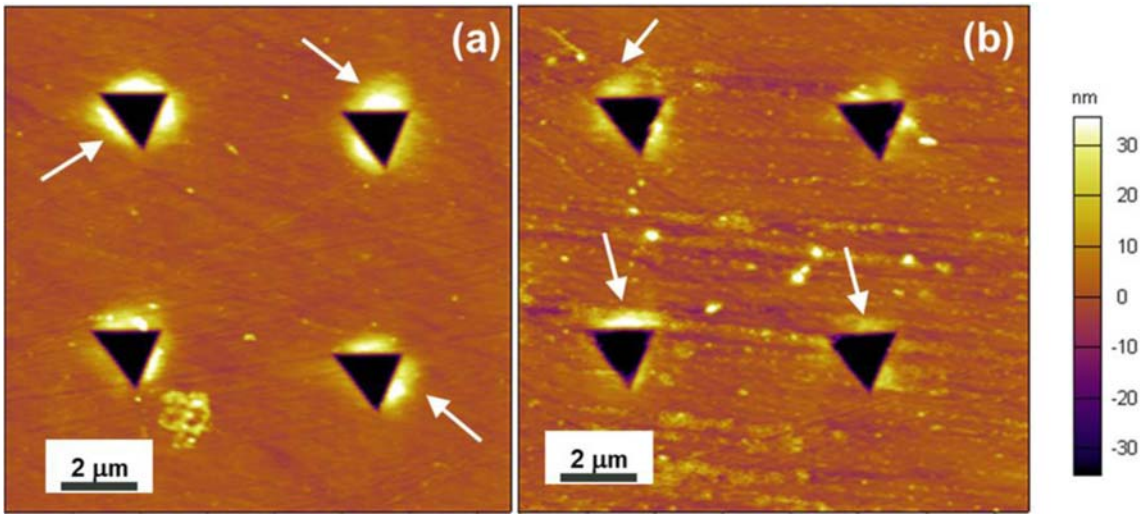

Fig. 6 AFM height maps of partial indentation arrays on the *yz* surface. **a** $z = 20$ mm. **b** $z = 0$ mm. Note that arrows point to typical pileup, which is more pronounced in the indents near the top ($z = 20$ mm) of the *yz* face. These pileups are likely caused by a higher degree of compressive residual stress in this location

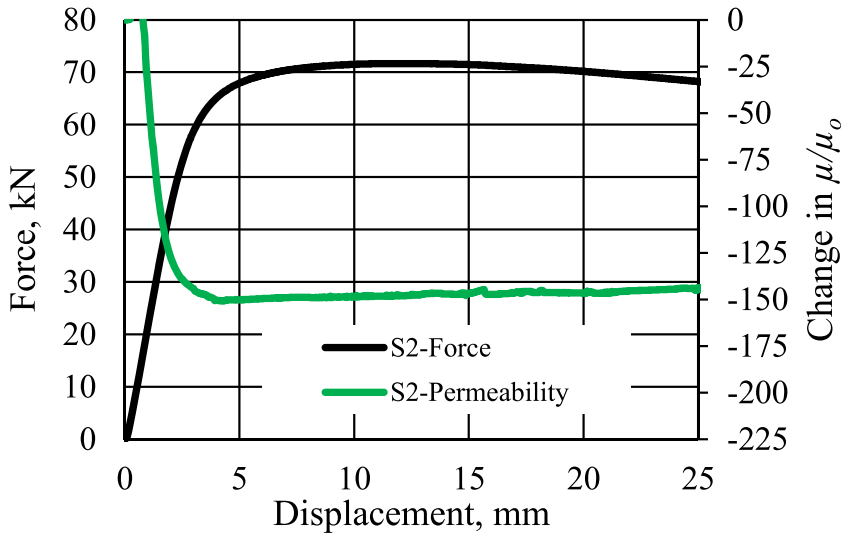

Fig. 7 Force-displacement and μ_r-displacement data for S2. Increases in force correspond to decreases in magnetic permeability (μ_r)

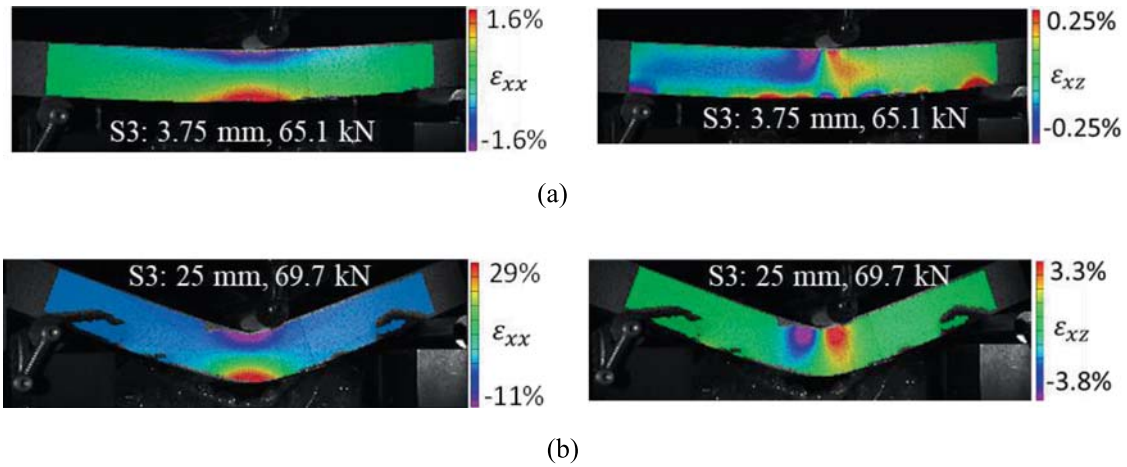

Fig. 8 DIC strain fields before and after significant yielding. Shadow artifacts at the correlation edges cause the data to become unresolved as the specimen is significantly deformed **a** Axial strain εxx and shear strain εxy DIC fields at 3.75 mm displacement and 65.1 kN force: S3. **b** Axial strain εxx and shear strain εxy DIC fields at 25 mm displacement and 69.7 kN force: S3

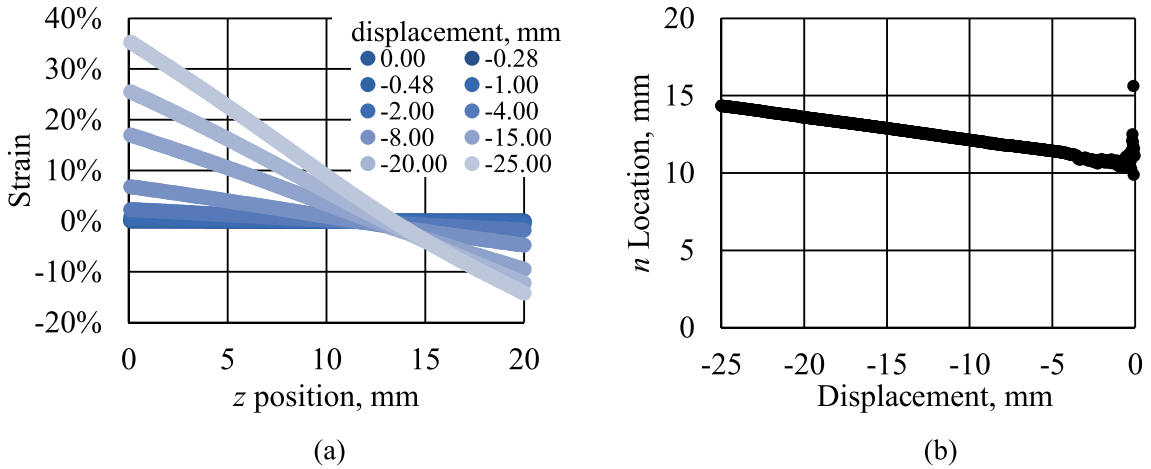

Fig. 9 **a** DIC axial strain extraction (S1) along the z direction under the top support as a function of displacement. **b** Under increasing displacement, tensile and compression strain become more asymmetric and the n location moves towards the top edge

from 0–50 kN with comparatively little change upon further loading from 50–70 kN.

All specimens did not fail during quasi-static loading up to 40 mm displacement. Each specimen was capable of significant plastic deformation, with microcracking only barely visible on the tension side. Asymmetric strain values were observed above 5 mm displacement; i.e., at 25 mm displacement, the axial tensile strain was around 29% at the bottom and − 11% at the top of the specimen (Fig. 8). The neutral axis (n) location, where the strain is zero, was not at the center of the specimen after general yielding in the material (beyond around 3 mm displacement). The n location was biased towards the compression side of the specimen and became more biased with increased displacement (Fig. 9). DIC is typically not able to resolve the exact edge of a specimen; therefore, the location of n may vary somewhat from Fig. 9 depending on the correlation of the top and bottom edges being assumed of equal quality.

This result suggests that the compression and tension moduli of the material were not identical, which was not expected. This result is due to uneven plastic deformation behavior in compression and tension likely due to an artifact of the LPBF process, i.e., microscale material property differences or residual stress distribution through-the-thickness. The difference in compression and tension moduli requires that the equations for determining stress be modified to take into account the imbalance. Derivations of Eqs. 1 and 2 are straightforward, especially when the strain response is linear involving force and moment balancing available in mechanics textbooks. Geometry symbols are illustrated in Fig. 1 with F representing the applied load.

$$\sigma_t = \frac{3FL_s}{4wnt} \tag{1}$$

$$\sigma_c = \frac{n}{t-n}\sigma_t \tag{2}$$

The modified stress-strain behavior is shown in Fig. 10 with modulus (E), yield (σ_y), and maximum stress (σ_{max}) measurements of 189 GPa (C_v 9.2%), 1370 MPa (C_v 8.4%), and 1750 MPa (C_v 3.0%) for tension, respectively, and 235 GPa (C_v 4.2%), 1620 MPa (C_v 3.8%), and 3360 MPa (C_v 6.0%) for compression, respectively, on average. Yield strength is measured as the 0.2% offset value, maximum stress is the largest stress measured, and modulus is reported as a fit to the 1000–4000 με range. There is no strain to failure measurement as the specimens did not break.

5.2 Fatigue loading

Fatigue loading was conducted in force control by targeting a peak value in the range of 30–60 kN, resulting in the range of

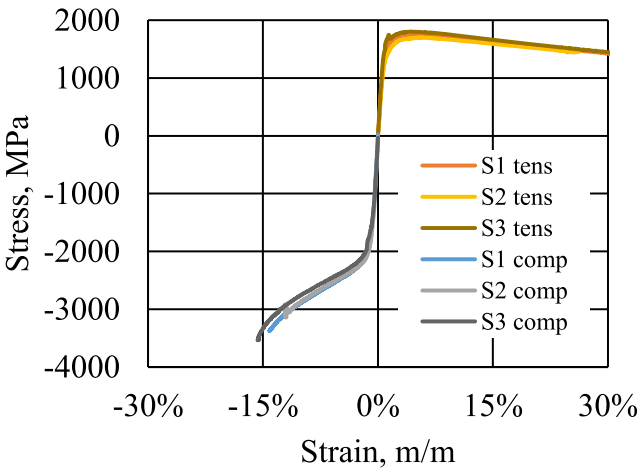

Fig. 10 Stress-strain response compensated for asymmetry in compression and tension behavior based on DIC measurements from the three-point bending test

Table 1 Summary of test measurements for quasi-static and fatigue testing

Number	μ_r at zero load		Compression measurement			Tension measurement			Fatigue	
	x dir.	*y* dir.	*E*, GPa	σ_y, MPa	σ_{max}, MPa	*E*, GPa	σ_y, MPa	σ_{max}, MPa	*F*, *N*	Cycles
1			237.6	1650	3407	186.6	1317	1738	72,915	1
2			243.6	1660	3142	173.1	1262	1702	71,671	1
3			224.5	1553	3537	207.8	1479	1804	73,213	1
4	129	162							60,000	3782
5	128	174							60,000	3941
6	133	166							58,000	4787
7	130	184							56,000	6128
8	122	175							54,000	4656
9	131	188							50,000	5985
10	127	171							48,000	9040
11	131	182							46,000	8020
12	125	190							40,000	17,487
13	128	163							37,000	17,995
14	132	158							34,000	18,867
15	130	189							30,000	30,387

approximately 3×10^3 to 3×10^4 cycles (Table 1). A force of 50 kN corresponds to approximately the yield stress on the tension side of a specimen (1370 MPa, C_v 8.4%) but is likely complicated by movement of the location of *n* and accumulation of damage over time. In static loading, specimens were able to displace to 40 mm without failing, but under fatigue loading, displacements at failure were 2–4 mm, depending on the peak force.

DIC images collected over several cycles at various fractions of life showed that the strain distribution in the *z* direction was linear and asymmetric at early points in life, similar to Fig. 9, becoming increasingly nonlinear later in life. The neutral axis moved from the specimen center towards the compression side by as much as 1 mm at 90% of life, which was much lower than observed in static testing (Fig. 9). Axial strain extraction along the *z* direction under the center loading support showed significant strain asymmetry in tension and compression after approximately 75% of life, with a large strain concentration on the tension side at approximately 90% of life (Fig. 11).

The remaining useful life as measured by the DIC at peak tensile strain was sensitive to significant change after

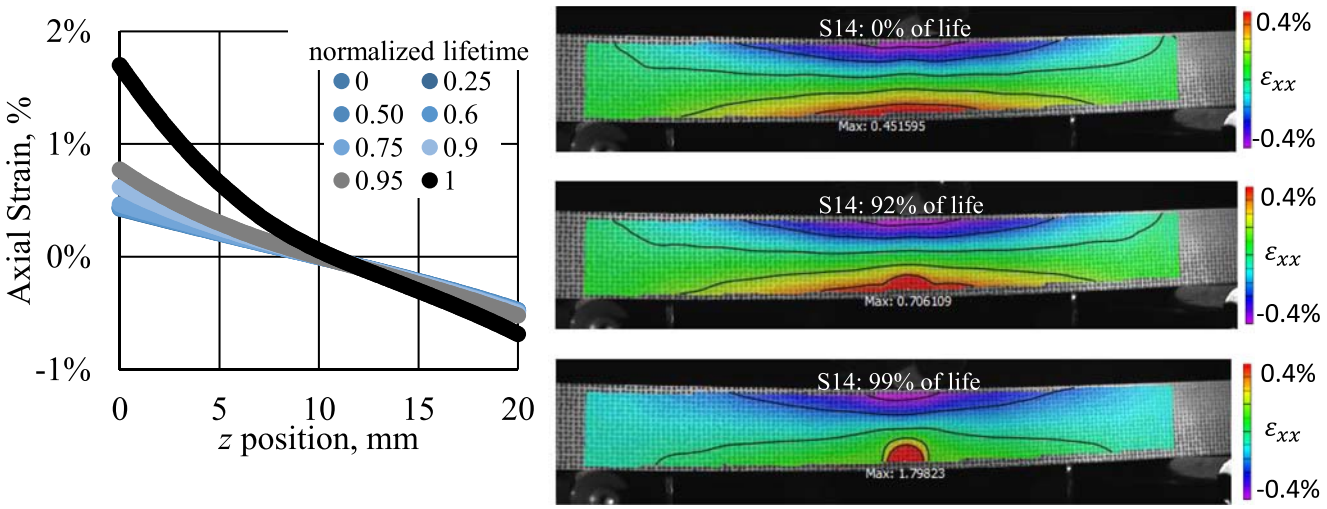

Fig. 11 S14 DIC axial strain extraction along the *y* direction under the top support and associated contour plots. The *n* starts biased towards the compression direction at 1–2 mm, increasing with cycles. At around 90% of life, significant yielding on the tension side of the sample was observed

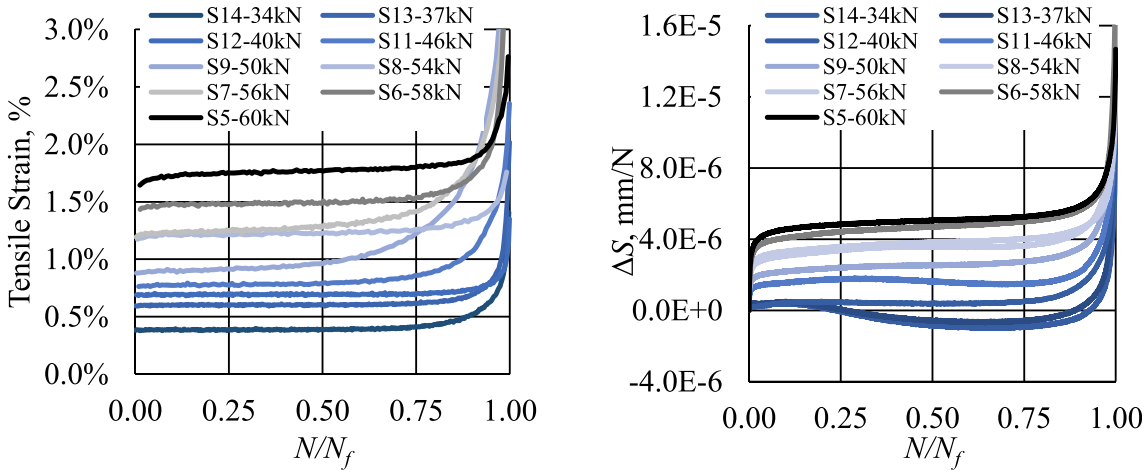

(a) DIC measurements (b) MTS measurements

Fig. 12 DIC measurements of peak tensile strain (**a**) and structural compliance (**b**) vs. various numbers of cycles (N) normalized to failure cycles (N_f). A gradient of behavior appears to exist comparing cycling above to below the yield strength for this relatively small data set

approximately 90% of life (Fig. 12a). The DIC was not able to reliably provide a signal for predicting life before 90%, unless the volume of material undergoing failure was in the observation plane, which is an expected result. Occasionally the DIC measured large changes in tensile strain as early as 60% of life, such as for specimens S7 and S9.

The structural compliance, calculated as $\Delta S_j = (d_j - d_1)/(F_j - F_1)$, describes the change in the force and displacement at cycle j compared with the initial force and displacement measured by the MTS frame. Compared with the DIC measurement, the structural compliance is a global measure that can be influenced by any member in the load path including the fixture. Structural compliance was more consistent than DIC but also only showed significant change at around 90% of life (Fig. 12b). The structural compliance also showed a slight stiffening effect when the fatigue load was significantly below the yield strength (e.g., the displacement necessary for the MTS controller to maintain the peak force was initially decreasing for much of the specimen life before increasing at failure). Strain measurement would provide a fatigue signal as early as 60% of life at the location of a critical feature; otherwise, a compliance measure of the whole structure could be used but would only be sensitive at around 90% of life.

The relative magnetic permeability μ_r for several different specimens is shown in Fig. 13 for the first loading cycle. The lowest value of μ_r corresponds to the peak force, which was seen to be asymptotic at around 40 kN in static loading (Fig. 7). The valley force, which here is always 10% of the peak with an R ratio of 0.1, is very different depending on whether or not the peak force was above 50 kN. This could be due to residual stress development or microstructural differences in the material caused by plastic damage that influences the eddy current response induced by the array.

The change in the μ_r signal over time was largely dependent on subsurface damage and eventually final fracture across the tensile side of the specimen. The eddy current response was more sensitive to life when damage was localized to where the array was placed; however, generally over time, the minimum and mean measurement increased (Fig. 14). The shape of the signal also changed, with a decreasing amplitude as damage accumulated in the material.

The remaining useful life as measured by μ_r was sensitive to significant change after approximately 60% of life when the peak force was greater than 50 kN and at approximately 80% of life when the peak force was less than 50 kN (Fig. 15). The sensitivity of this change was predicated upon colocation of the sensor and the final failure. Eddy current measurements were observed to be capable of approximating life based on peak μ_r signal change over time with increased sensitivity for larger cyclic forces.

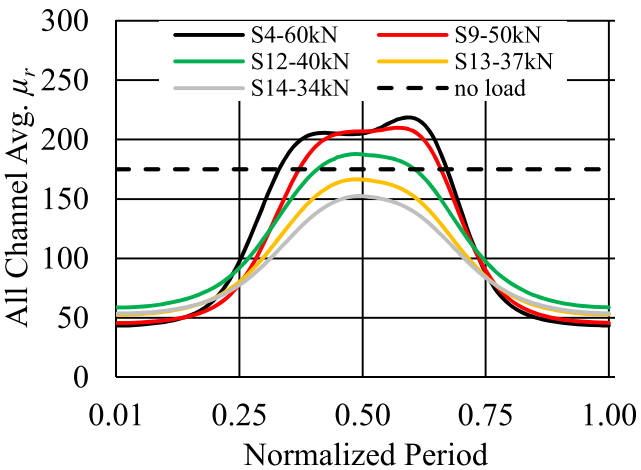

Fig. 13 Magnetic permeability μ_r over the first loading cycle for specimens of various peak force values. Peak force corresponds to lowest μ_r

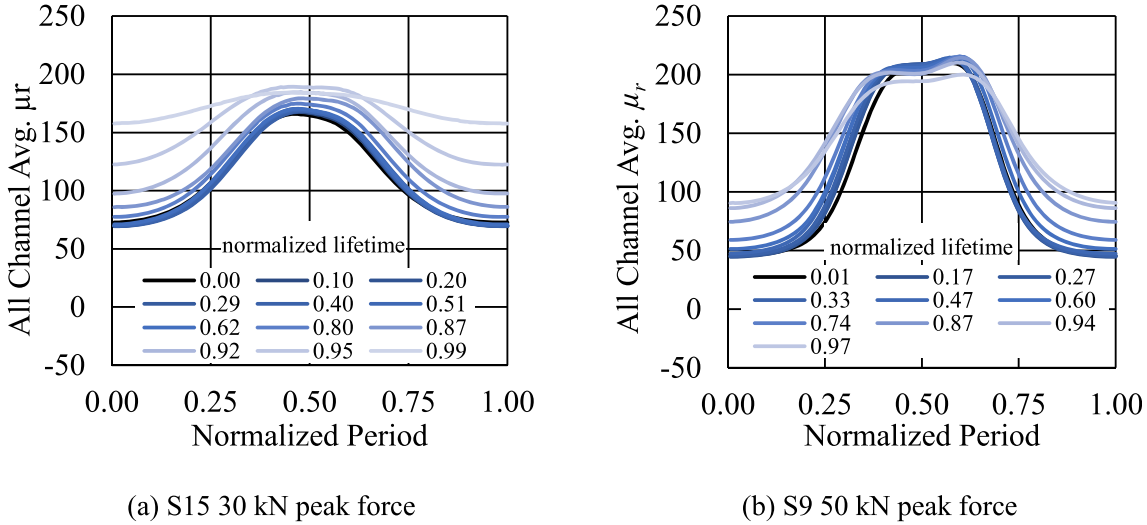

(a) S15 30 kN peak force (b) S9 50 kN peak force

Fig. 14 Magnetic permeability μ_r for successive cyclic periods at various points of life

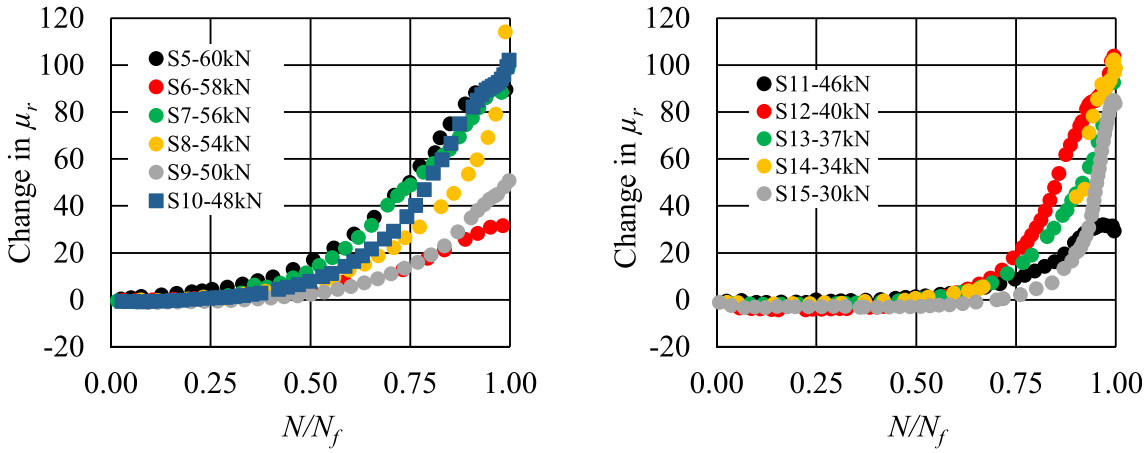

Fig. 15 Magnetic permeability μ_r after various numbers of cycles (N) normalized to failure cycles (N_f)

6 Conclusion

Ex situ evaluation of the AM maraging steel specimens, using X-ray computed tomography and atomic force microscopy, showed that there was relatively low porosity (0.34–0.36%) evenly distributed throughout the volume. Nano-indentation tests at $z = 20$ mm showed higher indentation modulus and hardness response with respect to tests performed at $z = 0$ mm, which was possibly due to increased residual compressive stress at the top of the specimens. Evaluation of the nano-indentation and porosity results supports a general consistency for the material at larger scales, which would lend itself to well the use of representative volume elements in stiffness simulations at larger scales. Simulation of fatigue or failure will require accurate representation of the microscale variation and porosity.

In situ measurements of the relative magnetic permeability μ_r and strain via DIC showed anisotropy in the material even under zero load in the build plane. Asymmetric strain amplitudes in compression and tension were observed with DIC under quasi-static loading possibly due to a different material response through the build direction of the part identified by nano-indentation and AFM. It may be that these measurements are manufacturing-parameter dependent; however, cognizance of their behavior is necessary for more complicated simulation and design. Experimental results indicate that specimens were able to support extensive displacement past yielding in static loading while failing after relatively low cyclic displacements (2–4 mm) in the range of 10–30 k cycles.

Measurements of structural compliance and DIC tensile strain over time were shown to be sensitive to damage at approximately 90% of life. DIC measurements were situationally more sensitive depending on colocation of failure and observation where structural compliance was consistently agnostic to failure location. Eddy current measurements were better able to capture the mechanical state as early as 60% of life depending also on failure location. Each method of measurement was able to report on the state of the AM material for

different points of life and given a relevant structural application, monitoring techniques could be focused in critical areas. With the experimental material-property-structure investigations contained in this work, parts could be designed to amplify the measurement signal by manipulating the print material in a way that would not be possible with traditional manufacturing techniques. This work contains the information necessary to formulate a multi-scale simulation incorporating microscale measurements as well as fatigue evolution characteristics for strain and relative magnetic permeability.

Acknowledgments The authors would like to acknowledge the manufacturing of experimental specimens tested in this work by Mr. Bradley Ruprecht, Mr. Rashad Scott, and Mr. Jack Spangler of the Edgewood Chemical Biological Center (ECBC). Mr. Scott Grendahl also assisted in the wire EDM of cylinder samples for X-ray CT. The raw/processed data required to reproduce these findings cannot be shared publically at this time as the data also forms part of an ongoing study but can be shared at request.

References

1. Yadollahi A, Shamsaei N (2017) Additive manufacturing of fatigue resistant materials: challenges and opportunities. Int J Fatigue 98: 14–31
2. Beretta S, Romano S (2017) A comparison of fatigue strength sensitivity to defects for materials manufactured by AM or traditional processes. Int J Fatigue 94:178–191
3. Flodberg G, Pettersson H, Yang L (2018) Pore analysis and mechanical performance of selective laser sintered objects. Additive Manufacturing 24:307–315
4. Gatto A, Bassoli E, Denti L (2018) Repercussions of power contamination on the fatigue life of additive manufactured maraging steel. Additive Manufacturing 24:13–19
5. Shamsaei N, Yadollahi A, Bian L, Thompson SN (2015) An overview of direct laser deposition for additive manufacturing; part II: mechanical behavior, process parameter optimization and control. Additive Manufacturing 8:12–35
6. Konecna R, Kunz L, Nicoletto G, Baca A (2016) Long fatigue crack growth in Inconel 718 produced by selective laser melting. Int J Fatigue 92:499–506
7. Hedayati R, Hosseini-Toudeshky H, Sadighi M, Mohammadi-Aghdam M, Zadpoor AA (2016) Computational prediction of the fatigue behavior of additively manufactured porous metallic biomaterials. Int J Fatigue 84:67–79
8. Walker KF, Liu Q, Brandt M (2017) Evaluation of fatigue crack propagation behavior in Ti-6Al-4V manufactured by selective laser melting. Int J Fatigue 104:302–308
9. Hedayati R, Hosseini-Toudeshky H, Sadighi M, Mohammadi-Aghdam, Zadpoor AA (2018) Multiscale modeling of fatigue crack propagation in additively manufactured porous biomaterials. Int J Fatigue 113:416–427
10. Bassoli E, Denti L, Comin A, Sola A, Tognoli E (2018) Fatigue behavior of as-built L-PBF A357.0 parts. Metals 8:634–647
11. Sarkar S, Kumar CS, Nath AK (2019) Investigation on the mode of failures and fatigue life of laser-based powder bed fusion produced stainless steel parts under variable amplitude loading conditions. Additive Manufacturing 25:71–83
12. Kirka MM, Greeley DA, Hawkins C, Dehoff RR (2017) Effect of anisotropy and texture on the low cycle fatigue behavior of Inconel 718 processed via electron beam melting. Int J Fatigue 105:235–243
13. Spierings AB, Starr TL, Wegener K (2013) Fatigue performance of additive manufactured metallic parts. Rapid Prototyp J 19:88–94
14. Lindberg A, Alfthan J, Pettersson H, Flodberg G, Yang L (2018) Mechanical performance of polymer powder bed fused objects-FEM simulation and verification. Additive Manufacturing 24: 577–586
15. Gomez-Gras G, Jerez-Mesa R, Travieso-Rodriguez JA, Lluma-Fuentes J (2018) Fatigue performance of fused filament fabrication PLA specimens. Mater Des 140:278–285
16. Puigoriol-Forcada JM, Alsina A, Salazar-Martin AG, Gomez-Gras G, Perez MA (2018) Flexural fatigue properties of polycarbonate fused-deposition modelling specimens. Mater Des 155:414–421
17. Van Hooreweder B, Moens D, Boonen R, Kruth JP, Sas P (2013) On the difference in material structure and fatigue properties of nylon specimens produced by injection molding and selective laser sintering. Polym Test 32:972–981
18. Van Hooreweder B, De Coninck F, Moens D, Boonen R, Sas P (2010) Microstructural characterization of SLS-PA12 specimens under dynamic tension/compression excitation. Polym Test 29: 319–326
19. Amel H, Moztarzadeh H, Rongong J, Hopkinson N (2014) Investigating the behavior of laser-sintered nylon 12 parts subject to dynamic loading. J Mater Res 29(3):319–326
20. Amel H, Rongong J, Moztarzadeh H, Hopkinson N (2016) Effect of section thickness on fatigue performance of laser sintered nylon 12. Polym Test 53:204–210
21. Croccolo D, De Agostinis M, Fini S, Olmi G, Robusto F, Kostic SC, Vranic A, Bogojevic N (2018) Fatigue response of as-built DMLS maraging steel and effects of aging, machining, and peening treatments. Metals 8:505–526
22. Suryawanshi J, Prashanth KG, Ramamurty U (2017) Tensile, fracture, and fatigue crack growth properties of a 3D printed maraging steel through selective laser melting. J Alloys Compd 725:355–364
23. Vandresse N, Ky I, Gonzalez FQ, Nuno N, Bocher P (2016) Image analysis characterization of periodic porous materials produced by additive manufacturing. Mater Des 92:767–778
24. Vandresse N, Richter A, Nuno N, Bocher P (2018) Measurement of deformation heterogeneities in additive manufactured lattice materials by digital image correlation: strain maps analysis and reliability assessment. J Mech Behav Biomed Mater 86:397–408
25. Takezawa A, Koizumi Y, Kobashi M (2017) High-stiffness and strength porous maraging steel via topology optimization and selective laser melting. Additive Manufacturing 18:194–202
26. Mezzadri F, Bouriakov V, Qian X (2018) Topology optimization of self-supporting support structures for additive manufacturing. Additive Manufacturing 21:666–682
27. Al-Ketan O, Rowshan R, Abu Al-Rub RK (2018) Topology-mechanical property relationship of 3D printed strut, skeletal, and sheet based periodic metallic cellular materials. Additive Manufacturing 19:167–183
28. Henry TC, Johnson TE, Haynes RA, Tran A (2021) Fatigue performance of polyamide 12 additively manufactured structures design with topology optimization. Journal of Testing and Evaluation 49(3). https://doi.org/10.1520/JTE20180793
29. Cole DP, Henry TC, Gardea F, Haynes RA (2017) Interphase mechanical behavior of carbon fiber reinforced polymer exposed to cyclic loading. Compos Sci Technol 151:202–210
30. Cole DP, Riddick JC, Jaim HMI, Strawhecker KE, Zander NE (2016) Interfacial mechanical behavior of 3D printed ABS. Appl Polym Sci 133(30):1–12
31. Sangid MD (2013) The physics of fatigue crack initiation. Int J Fatigue 57:58–72

32. Shih CC, Ho NJ, Huang HL (2010) The effects of grain boundary on dislocation development for cyclically deformed IF steel. Mater Sci Eng A 527:7247–7251
33. Basinksi ZS, Basinski SJ (1992) Fundamental aspects of low-amplitude cyclic deformation in face-centered cubic crystals. Prog Mater Sci 36:89–148
34. Habtour EM, Cole DP, Kube CM, Henry TC, Haynes RA, Gardea F, Sano T, Tinga T (2019) Structural state awareness through integration of global dynamic and local material behavior. J Intell Mater Syst Struct 30(9):1355–1365
35. Habtour E, Cole DP, Stanton SC, Sridharan R, Dasgupta A (2016) Damage precursor detection for structures subjected to rotational base vibration. Intl J Nonlinear Mech 82:49–58
36. Habtour E, Sridharan R, Dasgupta A, Robeson M, Vantadori S (2018) Phase influence of combined rotational and transverse vibrations on the structural response. Mech Syst Signal Process 100: 371–383
37. Kube C, Turner J (2015) Acoustic non-linearity parameters for transversely isotropic polycrystalline materials. J Acous Soc Am 137:3272–3280
38. Na JK, Oneida EK (2018) Nondestructive evaluation method for standardization of fused filament fabrication based additive manufacturing. Additive Manufacturing 24:154–165
39. Ziemian CW, Ziemian RD, Haile KV (2016) Characterization of stiffness degradation caused by fatigue damage of additive manufactured parts. Mater Des 109:209–218
40. Shi SB, Gu LX, Liang J, Fang BD, Gong CL, Dai CX (2016) A mesomechanical model for predicting the degradation in stiffness of FRP composites subjected to combined thermal and mechanical loading. Mater Des 89:1079–1085
41. Ghanei S, Kashefi M, Mazinani M (2013) Eddy current nondestructive evaluation of dual phase steel. Mater Des 50:491–496
42. Cherry MR, Sathish S, Mooers RD, Pilchak AL, Grandhi R (2017) Modeling of the change of impedance of an eddy current probe due to small changes in host conductivity. IEEE Trans Magn 53(5):1–10
43. Garcia-Martin J, Gomez-Gil J, Vazquez-Sanchez E (2011) Non-destructive techniques based on eddy current testing. Sensors 11(3):2525–2565
44. Tang M, Pistorious PC, Beuth JL (2017) Prediction of lack-of-fusion porosity for powder bed fusion. Additive Manufacturing 14:39–48
45. Oliver WC, Pharr GM (1992) An improved technique for determining hardness and elastic modulus using load displacement sensing indentation experiments. J Mater Res 7(6):1564–1583
46. Lee YH, Kwon D (2003) Measurement of residual stress effect by nanoindentation on elastically strained (100) W. Scr Mater 49(5): 459–465